Applied Nanoscience (2020) 10:3103–3113
https://doi.org/10.1007/s13204-019-01028-y

ORIGINAL ARTICLE

Nonlinear radiative heat flux in Oldroyd-B nanofluid flow with Soret and Dufour effects

Tasawar Hayat[1,2] · Madiha Rashid[1] · Ahmed Alsaedi[2]

Received: 28 January 2019 / Accepted: 2 April 2019 / Published online: 4 May 2019

Abstract

Present paper investigates the flow of Oldroyd-B nanofluid due to stretching cylinder. Heat transfer aspects are expressed by nonlinear radiation and non-uniform heat source/sink. Analysis of Soret and Dufour effects are emphasized. Brownian movement and thermophoresis phenomena are retained. Characteristics of mass transfer subject to first-order chemical reaction is examined. Consideration of suitable transformations yields ordinary differential systems. Relevant problem is solved by Optimal homotopic approach. The concept of minimization is employed by defining the average squared residual errors. Behavior of various physical variables on dimensionless velocity, temperature and concentration fields are determined. In addition, the rates of heat and mass transfer are studied through graphs. Here, we noticed a growth in velocity, temperature and concentration for larger values of curvature parameter.

Keywords Oldroyd-B nanofluid · Non-uniform heat source/sink · Nonlinear thermal radiation · Soret and Dufour effects · Chemical reaction

Introduction

Nanofluids containing nanomaterials such as metallic oxides, copper, silver and carbides have greater thermal conductivity to that of conventional base fluid. Water, engine oil and ethylene glycol are commonly used heat transfer fluids. Nanofluid can effectively be used for a wide range of mechanical industrial processes such as glass fiber innovation, melt spinning, microprocessors, chillers and hybrid power engine. Choi (1995) introduced nanofluid containing nanoparticles in base fluid to enhance their thermal properties. Then, Buongiorno (2006) developed the mathematical model for convective transport of nanofluids. The present model contains two elements, namely Brownian motion and thermophoresis parameter which are very important in nanofluids. Brownian motion is random motion of particles in a fluid due to their collision with molecules of water. Nanofluid flow over a stretching sheet with thermophoresis and Brownian motion effects has been discussed by Babu and Sandeep (2016). Reddy et al. (2017) studied the flow of Williamson nanofluid due to stretching sheet with variable thickness. Recent developments about nanofluid are cited in Khan et al. (2017), Munyalo and Zhang (2018), Madavan et al. (2018), Minakov et al. (2018), Hayat et al. (2018a), Khan et al. (2018) and Irfan and Khan (2019).

Most of the researches are limited to fluids which obey Newtonian postulate and cannot predict the elastic characteristics. Many industrial and geophysical processes such as petroleum drilling, pulps, polymers, slurries, pastes and complex mixtures involve viscoelastic fluids which examine both viscosity and elasticity. Viscoelastic fluids are subclasses of non-Newtonain fluids. Oldroyd-B fluid model is a significant rate type viscoelastic fluid which can simultaneously specify the features of relaxation and retardation. The rate type viscoelastic fluids carry one or more time derivatives in extra stress tensors. Bhatnagar et al. (1995) presented the flow of an Oldroyd-B fluid model. Heat transfer in the flow of an Oldroyd-B fluid due to stretching surface of decreasing index has been studied by Hayat et al. (2017). Rasheed and Anwar (2018) worked on fractional nonlinear viscoelastic fluid flow. Relaxation–retardation characteristics of Oldroyd-B fluid with

✉ Madiha Rashid
madiha.rashid@math.qau.edu.pk

1 Department of Mathematics, Quaid-I-Azam University, 45320, Islamabad 44000, Pakistan

2 Nonlinear Analysis and Applied Mathematics (NAAM) Research Group, Department of Mathematics, Faculty of Science, King Abdulaziz University, Jeddah 21589, Saudi Arabia

viscous dissipation and chemical reaction are given by Zhang et al. (2018). Farooq et al. (2018) discussed three-dimensional Oldroyd-B fluid with Soret and Dufour effects. Chemical reacting species in a fractional viscoelastic fluid flow has been developed by Rasheed and Anwar (2019).

Nowadays, much attention has been focused on fluid flows caused by stretching cylinder with Soret and Dufour effects. When the phenomena of heat and mass transport occur simultaneously in liquid motion, then relations between driving potentials and enthalpy and mass fluxes are highly complicated. It is worth mentioning that not only does the temperature gradient produce heat flux, but also it is caused by the concentration gradient as well. Dufour effects describe the diffusion of heat transport via the concentration gradient, while Soret effects describe the temperature gradient that can cause mass flux. In many cases, these effects were often neglected due to their smaller magnitude in comparison with effects indicated by Fourier's and Fick's laws. Significant applications of Soret and Dufour effects in hydrology and petrology include solidification of binary alloys, isotope separation, groundwater pollutant migration, chemical reactors and geosciences multi-component melts. Nishimura et al. (1998) proposed a model of combined horizontal temperature and concentration gradients in a rectangular enclosure. The impact of non-uniform heated plate on double-diffusive natural convection of micropolar fluid in a square cavity with Soret and Dufour effects is given by Muthtamilselvan et al. (2018). Mudhaf et al. (2018) worked on the flow of natural convection in porous trapezoidal enclosures with Soret and Dufour effects. Oldroyd-B nanofluid flow due to stretching cylinder was investigated by Khan et al. (2019).

The main objective of the present article is to discuss the chemically reactive flow of Oldroyd-B nanofluid with heat and mass transfer mechanisms. The consequences of Brownian motion and thermophoresis diffusion in viscoelastic nanofluid due to stretching cylinder were examined. The influence of nonlinear radiative heat flux, internal heat generation/absorption and Soret and Dufour effects were also incorporated in detail. Reduced coupled nonlinear ordinary differential system was solved by OHAM (Awais et al. 2016; Anwar and Rasheed 2017; Gupta et al. 2018; Anwar and Rasheed 2018; Awais et al. 2018; Hayat et al. 2018b, c; Abel et al. 2012; Megahed 2013). The best optimal values of convergence control parameters are awarded in terms of numerical and graphical illustrations to study the emerging physical variables.

Modeling

Here, two-dimensional axisymmetric flow of viscoelastic fluid obeying Oldroyd-B model due to stretching cylindrical sheet is examined. The contributions due to Brownian movement and thermophoresis phenomena are also explored. Soret and Dufour effects are accounted in a given flow configuration. The aspects of nonlinear radiation, first-order chemical reaction and non-uniform heat source/sink are imposed. Cylindrical coordinates (r, z) are used to model the relevant equations. Flow is initiated due to a stretching cylinder with velocity $w_{\mathrm{w}} = w_0\left(\frac{z}{L}\right)$ in the axial direction. Coordinate systems and geometry of the problem are shown in Fig. 1.

The relevant flow problem satisfies (Irfan et al. 2018; Alshomrani et al. 2018):

$$\frac{\partial u}{\partial r} + \frac{u}{r} + \frac{\partial w}{\partial z} = 0, \tag{1}$$

$$\begin{aligned} u\frac{\partial w}{\partial r} + w\frac{\partial w}{\partial z} + \lambda_1\left[w^2\frac{\partial^2 w}{\partial z^2} + u^2\frac{\partial^2 w}{\partial r^2} + 2uw\frac{\partial^2 w}{\partial r\partial z}\right] = \nu\left[\frac{\partial^2 w}{\partial r^2} + \frac{1}{r}\frac{\partial w}{\partial r}\right] \\ +\nu\lambda_2\left[\frac{u}{r^2}\frac{\partial w}{\partial r} - \frac{1}{r}\frac{\partial w}{\partial r}\frac{\partial w}{\partial z} - \frac{2}{r}\frac{\partial u}{\partial r}\frac{\partial w}{\partial r} + \frac{w}{r}\frac{\partial^2 w}{\partial r\partial z} - \frac{\partial w}{\partial r}\frac{\partial^2 w}{\partial r\partial z} - 2\frac{\partial w}{\partial r}\frac{\partial^2 u}{\partial r^2}\right. \\ \left. + \frac{u}{r}\frac{\partial^2 w}{\partial r^2} - \frac{\partial w}{\partial z}\frac{\partial^2 w}{\partial r^2} - w\frac{\partial^3 w}{\partial r^2\partial z} + u\frac{\partial^3 w}{\partial r^3}\right], \end{aligned} \tag{2}$$

$$\begin{aligned} & u\frac{\partial T}{\partial r} + w\frac{\partial T}{\partial z} \\ & = \alpha_1\left[\frac{\partial^2 T}{\partial r^2} + \frac{1}{r}\frac{\partial T}{\partial r}\right] + \tau\left[D_{\mathrm{B}}\frac{\partial C}{\partial r}\frac{\partial T}{\partial r} + \frac{D_{\mathrm{T}}}{T_\infty}\left(\frac{\partial T}{\partial r}\right)^2\right] \\ & - \frac{1}{\left(\rho C_{\mathrm{p}}\right)}\frac{1}{r}\frac{\partial}{\partial r}(rq) + \frac{D_{\mathrm{B}}K_{\mathrm{T}}}{\mu C_{\mathrm{p}}C_{\mathrm{s}}}\left(\frac{\partial^2 C}{\partial r^2} + \frac{1}{r}\frac{\partial C}{\partial r}\right) + \frac{1}{\left(\rho C_{\mathrm{p}}\right)}Q''', \end{aligned} \tag{3}$$

$$\begin{aligned} u\frac{\partial C}{\partial r} + w\frac{\partial C}{\partial z} = D_{\mathrm{B}}\left[\left(\frac{\partial^2 C}{\partial r^2} + \frac{1}{r}\frac{\partial C}{\partial r}\right)\right] + \frac{D_{\mathrm{T}}}{T_\infty}\left[\left(\frac{\partial^2 T}{\partial r^2} + \frac{1}{r}\frac{\partial T}{\partial r}\right)\right] \\ + \frac{D_{\mathrm{B}}K_{\mathrm{T}}}{T_\infty}\left(\frac{\partial^2 T}{\partial r^2} + \frac{1}{r}\frac{\partial T}{\partial r}\right) - K_{\mathrm{c}}\left(C - C_\infty\right), \end{aligned} \tag{4}$$

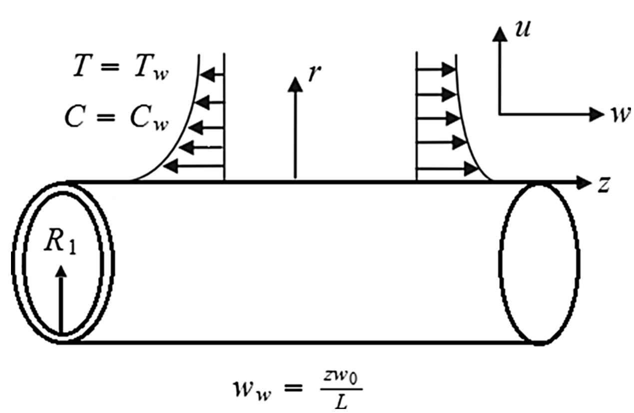

Fig. 1 Geometry of the problem

where $(w,\ u)$ are the components of velocity in z and r directions, respectively, λ_1 is the relaxation time, λ_2 is the retardation time, ν is the kinematic viscosity, $\alpha_1=\frac{k}{(\rho C_p)}$ is the thermal diffusivity, T is the temperature, $\tau=\frac{(\rho C_p)}{(\rho C_f)}$ is the heat capacity ratio, D_B is the Brownian diffusion coefficient, D_T is the thermophoresis diffusion coefficient, C is the nanoparticle volume fraction, μ is the dynamic viscosity, ρ is the fluid density, C_p is the specific heat, C_s is the concentration susceptibility and K_c is the chemical reaction rate. The nonlinear radiative heat flux is given by

$$q=-\frac{4\sigma^*\partial T^4}{3k^*\partial r}=-\frac{16\sigma^*}{3k^*}T^3\frac{\partial T}{\partial r}, \tag{5}$$

where σ^* and k^* are the Stefan–Boltzmann and Rosseland mean absorption coefficient, respectively. Utilizing Eqs. (5) in (3) we have

$$u\frac{\partial T}{\partial r}+w\frac{\partial T}{\partial z}=\alpha_1\left[\frac{\partial^2 T}{\partial r^2}+\frac{1}{r}\frac{\partial T}{\partial r}\right]+\tau\left[D_B\frac{\partial C}{\partial r}\frac{\partial T}{\partial r}+\frac{D_T}{T_\infty}\left(\frac{\partial T}{\partial r}\right)^2\right]+\frac{1}{(\rho C_p)_f}\frac{16\sigma^*}{3k^*}\frac{1}{r}\frac{\partial}{\partial r}\left(rT^3\frac{\partial T}{\partial r}\right)+\frac{1}{(\rho C_p)}Q'''. \tag{6}$$

The non-uniform heat source/sink is modeled as:

$$Q'''=\left(\frac{kw_w}{z\nu}\right)\left[A^*\left(T_w-T_\infty\right)f'+\left(T-T_\infty\right)B^*\right], \tag{7}$$

where A^* and B^* are parameters of the space-dependent and temperature-dependent internal heat generation/absorption, respectively. The case corresponds to internal heat generation when $(A^*>0)$ and $(B^*>0)$, and correspond to internal heat absorption when $(A^*<0)$ and $(B^*<0)$.

The associated boundary conditions are

$$u=0,\ v=0,\ w=w_w=\frac{zw_0}{L},\ T=T_w,\ C=C_w,\ \text{at } r=R_1,\quad w\to w_\infty,\ T\to T_\infty,\ C\to C_\infty,\ \text{as } r\to\infty. \tag{8}$$

Selecting

$$u=-\frac{R_1}{r}\sqrt{\frac{\nu w_0}{L}}f(\xi),\ w=\frac{zw_0}{L}f'(\xi),\ \theta(\xi)=\frac{T-T_\infty}{T_w-T_\infty},\quad \phi(\xi)=\frac{C-C_\infty}{C_w-C_\infty},\ \xi=\frac{r^2-R_1^2}{2R_1}\sqrt{\frac{w_0}{L\nu}}. \tag{9}$$

Equations (2), (3) and (6) take the form

$$(1+2\alpha\xi)f'''+2\xi f''+ff''-f'^2+2\beta_1 ff'f''-\beta_1 f^2f'''-\frac{\xi\beta_1}{(1+2\xi\eta)}f^2f''+(1+2\alpha\eta)\beta_2(f''^2-ff^{iv})-4\alpha\beta_2 ff'''=0, \tag{10}$$

$$\frac{1}{Pr}\left[\left(1+R\left(\theta\left(\theta_w-1\right)+1\right)^3\right)\left((1+2\alpha\xi)\theta''+2\alpha\theta'\right)\right]+\frac{3R}{Pr}\left[\left(\theta\left(\theta_w-1\right)+1\right)^2\left(\theta_w-1\right)(1+2\alpha\xi)\theta'^2\right]+f\theta'+(1+2\alpha\eta)Nb\theta'\phi'+(1+2\alpha\eta)Nt\theta'^2+\left(q_1f'+q_2\theta\right)+D_f\left((1+2\alpha\xi)\phi''+2\alpha\phi'\right)=0, \tag{11}$$

$$(1+2\alpha\eta)\phi''+2\alpha\phi'+Scf\phi'+\left(\frac{Nt}{Nb}+S_rS_c\right)\left((1+2\alpha\xi)\theta''+2\alpha\theta'\right)-ScC_r\phi=0, \tag{12}$$

$$f(0)=0,\ f'(0)=1,\ \theta(0)=1,\ \phi(0)=1, \tag{13}$$

$$f'(\infty)=0,\ \theta(\infty)=0,\ \phi(\infty)=0, \tag{14}$$

where $\beta_1=\frac{w_0\lambda_1}{L}$ is the Deborah number with respect to relaxation time, $\beta_2=\frac{w_0\lambda_2}{L}$ the Deborah number with respect to retardation time, $Pr=\frac{(\mu C_p)}{k}$ the Prandtl number, $R=\frac{16\sigma^* T_\infty^3}{3k^*k}$ the radiation parameter, $Nb=\frac{\tau(C_w-C_\infty)D_B}{\nu}$ the Brownian motion parameter, $Nt=\frac{\tau(T_w-T_\infty)D_T}{T_\infty\nu}$ the thermophoresis parameter, $S_r=\frac{D_BK_T(T_w-T_\infty)}{(C_w-C_\infty)\nu T_\infty}$ the Soret number, $D_f=\frac{D_BK_T(C_w-C_\infty)}{(T_w-T_\infty)C_pC_s}$ the Dufour number, $C_r=\frac{LK_c}{w_0}$ the chemical reaction parameter, $Sc=\frac{\nu}{D_B}$ the Schmidt number, and the curvature parameter $\alpha=\sqrt{\frac{L\nu}{w_0R_1^2}}$. It is worth pointing here that governing problem reduces to the Maxwell fluid case when $\beta_2=0$. Moreover, the analysis for the Newtonian model can be retrieved by selecting $\beta_1=0$.

Quantities of interest

Nusselt number

Mathematically,

$$Nu=\frac{zq_w}{k\left(T_w-T_\infty\right)}, \tag{15}$$

where wall heat flux is

$$q_w=-k\left(\frac{\partial T}{\partial r}\right)_{r=R_1}+\frac{16\sigma^*T^3}{3k^*}\left(\frac{\partial T}{\partial r}\right)_{r=R_1}, \tag{16}$$

and dimensionless expression of Nu is

$$Re_z^{-1/2}Nu=-\left[1+R\left(\theta_w\right)^3\right]\theta'(0). \tag{17}$$

Sherwood number

$$Sh = \frac{j_{\mathrm{w}}}{D_{\mathrm{B}}\left(C_{\mathrm{w}} - C_{\infty}\right)}, \tag{18}$$

where the wall mass flux is

$$j_{\mathrm{w}} = -D_{\mathrm{B}}\left(\frac{\partial C}{\partial r}\right)_{r=R_1}, \tag{19}$$

and the dimensionless expression of Sh is

$$Re_z^{-1/2} Sh = -\phi'(0), \tag{20}$$

in which the local Reynolds number is $Re_z = zw_w(z)/\nu$.

Solution methodology

With the aim of computing the solutions, the best optimal values are determined using optimal (OHAM). We define the initial guess for both $\left(f_0,\ \theta_0,\ \phi_0\right)$ and $\left(\mathcal{L}_f,\ \mathcal{L}_\theta,\ \mathcal{L}_\phi\right)$ as

$$f_0(\xi) = 1 - \exp(-\xi),\ \theta_0(\xi) = \exp(-\xi),\ \phi_0(\xi) = \exp(-\xi), \tag{21}$$

with

$$\mathcal{L}_f = f''' - f',\ \mathcal{L}_\theta = \theta'' - \theta,\ \mathcal{L}_\phi = \phi'' - \phi, \tag{22}$$

and

$$\begin{aligned} &\mathcal{L}_f\left[\mathring{C}_1 + \mathring{C}_2 \exp(-\xi) + \mathring{C}_3 \exp(\xi)\right] = 0, \\ &\mathcal{L}_\theta\left[\mathring{C}_4 \exp(\xi) + \mathring{C}_5 \exp(-\xi)\right] = 0, \\ &\mathcal{L}_\phi\left[\mathring{C}_6 \exp(\xi) + \mathring{C}_7 \exp(-\xi)\right] = 0, \end{aligned} \tag{23}$$

where the arbitrary constants are $\mathring{C}\ (i = 1 - 7)$.

Optimal convergence control variables

Non-zero auxiliary parameters $\hbar_f, \hbar_\theta$ and $\hbar_\phi$ define the convergence region of the homotopy series solutions. Minimization concept is applied for obtaining the best optimal data of $\hbar_f, \hbar_\theta$ and $\hbar_\phi$ by taking averaged squared residual errors as deliberated by

$$\varrho_m^f = \frac{1}{k+1}\sum_{l=0}^{k}\left[\mathcal{N}_f\left(\sum_{i=0}^{m} f(\xi),\ \sum_{i=0}^{m}\theta(\xi)\right)_{\xi=l\delta\xi}\right]^2, \tag{24}$$

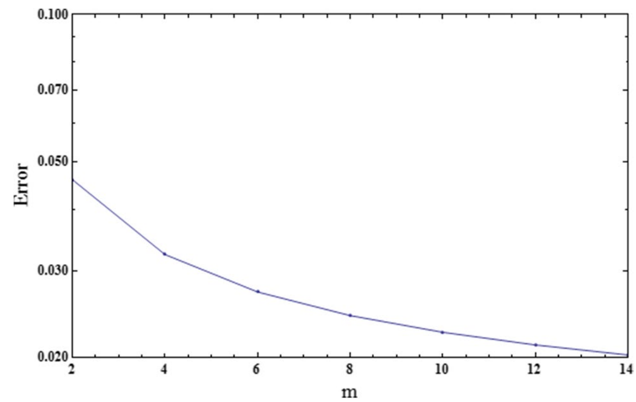

Fig. 2 Total error for Oldroyd-B fluid

Table 1 Optimal convergence control parameters and total averaged squared residual errors using BVPh 2.0

m	ε_m^f	ε_m^θ	ϱ_m^ϕ	CPU time (s)
2	1.2865×10^{-4}	7.9662×10^{-3}	434129×10^{-2}	2.39014
4	9.13899×10^{-5}	1.07799×10^{-3}	2.46443×10^{-2}	12.5917
6	7.02702×10^{-5}	3.18368×10^{-4}	1.80693×10^{-2}	26.7115
8	5.70706×10^{-5}	1.63694×10^{-4}	1.49369×10^{-2}	57.6813
10	4.81196×10^{-5}	7.63330×10^{-5}	1.30237×10^{-2}	123.245
12	4.16684×10^{-5}	6.30400×10^{-5}	116805×10^{-2}	264.350
14	3.68024×10^{-5}	4.37033×10^{-5}	106598×10^{-2}	542.276

$$\varrho_m^\theta = \frac{1}{k+1}\sum_{l=0}^{k}\left[\mathcal{N}_\theta\left(\sum_{i=0}^{m} f(\xi),\ \sum_{i=0}^{m}\theta(\xi),\ \sum_{i=0}^{m}\phi(\xi)\right)_{\xi=l\delta\xi}\right]^2, \tag{25}$$

$$\varrho_m^\phi = \frac{1}{k+1}\sum_{l=0}^{k}\left[\mathcal{N}_\phi\left(\sum_{i=0}^{m} f(\xi),\ \sum_{i=0}^{m}\theta(\xi),\ \sum_{i=0}^{m}\phi(\xi)\right)_{\xi=l\delta\xi}\right]^2, \tag{26}$$

$$\varrho_m^t = \varrho_m^f + \varrho_m^\theta + \varrho_m^\phi, \tag{27}$$

where $\varrho_m^t = 0.0515078$ represents the total squared residual error, $\delta\xi = 0.5$ and $k = 20$. The best optimal values of convergence control variables are $\hbar_f = -1.21023$, $\hbar_\theta = -1.19268$ and $\hbar_\phi = -1.47231$. Table 1 highlights the averaged residual errors with optimal values. A decline is observed for higher order of approximations. Plot for residual error is sketched in Fig. 2.

Table 2 Comparison of $-f''(0)$ in limiting sense for different values of β_1 when $\alpha = \beta_2 = 0$

β_1	$-f''(0)$		
	Ref. (Hayat et al. 2018b)	Ref. (Abel et al. 2012)	Present
0.0	1.000000	0.999978	1.000000
0.2	1.051948	1.051945	1.051949
0.4	1.101850	1.101848	1.101843
0.6	1.150163	1.150160	1.150155
0.8	1.196692	1.196690	1.196685
1.2	1.285257	1.285253	1.285247
1.6	1.368641	1.368641	1.368638
2.0	1.447617	1.447616	1.447619

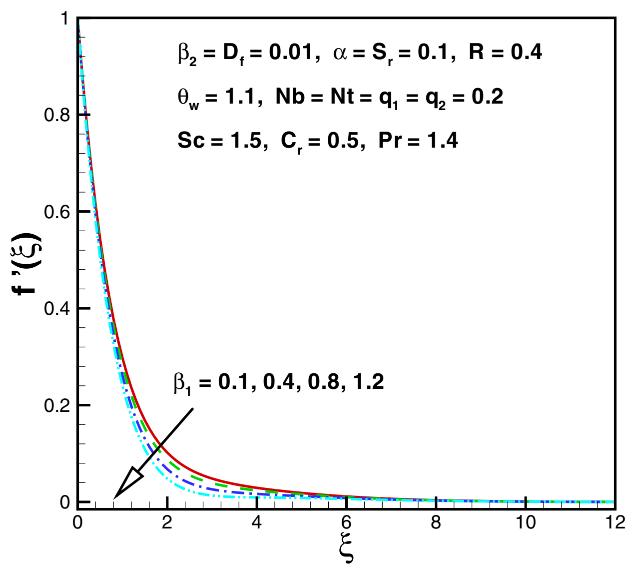

Fig. 3 Impact of β_1 on $f'(\xi)$

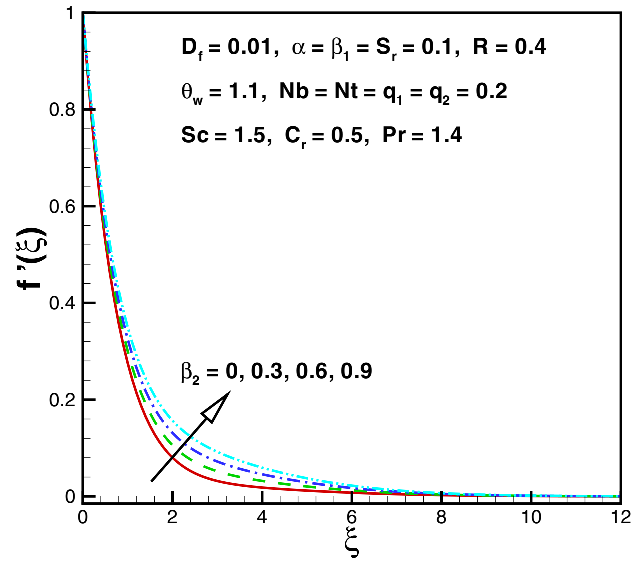

Fig. 4 Impact of β_2 on $f'(\xi)$

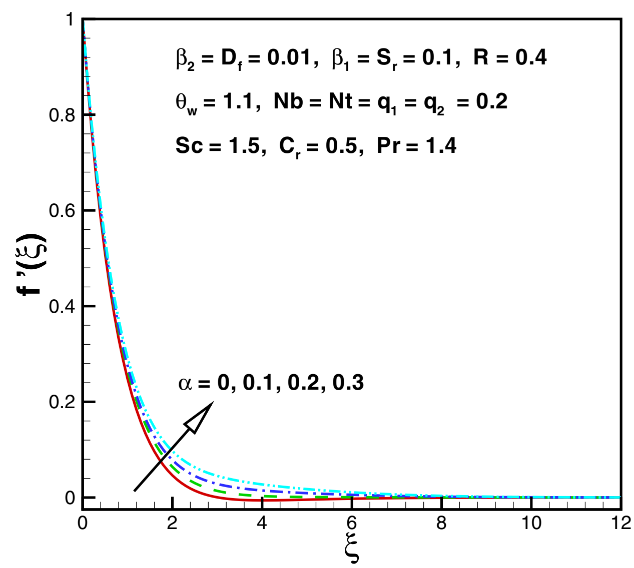

Fig. 5 Impact of α on $f'(\xi)$

Discussion

This section provides the graphical outlook on the effects of significant flow variables on velocity, temperature, concentration, Nusselt number $\left(Re_z^{\frac{-1}{2}} Nu\right)$ and Sherwood number $\left(Re_z^{\frac{-1}{2}} Sh\right)$. The optimal homotopy technique is implemented. Table 2 is prepared to give a comparison of $(-f''(0))$ in limiting cases with those of Hayat et al. (2018b) and Abel et al. (2012).

Velocity

Figure 3 is sketched to examine the the influence of Deborah number $(\beta_1 = 0.1, 0.4, 0.8, 1.2)$ on velocity. Here, we have noticed that the velocity of the fluid reduces gradually for higher (β_1). Physically, Deborah number (β_1) is the ratio of the timescale of the material response to observation timescale. We can judge the polymeric behavior of a material from three different cases. When $(\beta_1 << 1)$ the material is purely viscous, when $(\beta_1 >> 1)$ the material is elastic like, and when $(\beta_1 = 1)$ the material is viscoelastic. For higher

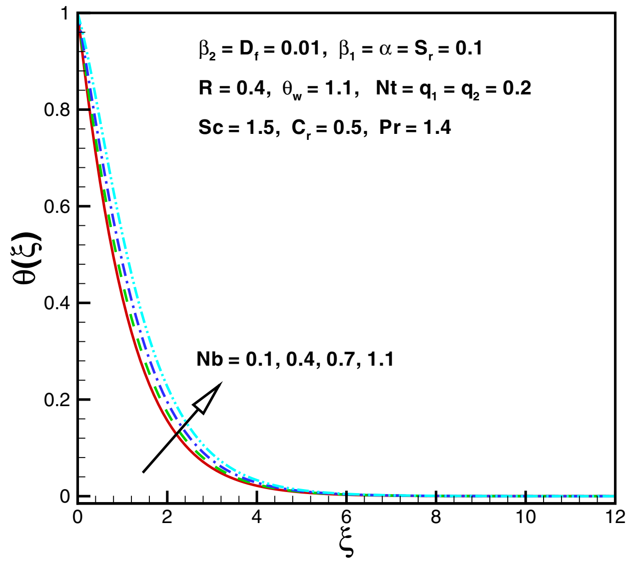

Fig. 6 Impact of Nb on $\theta(\xi)$

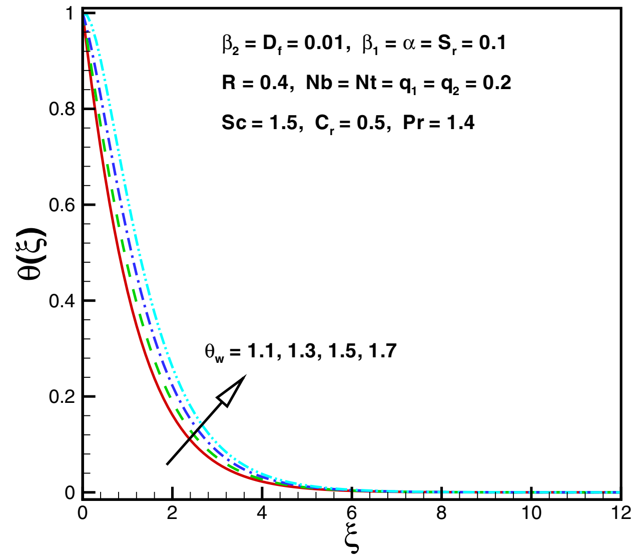

Fig. 8 Impact of θ_w on $\theta(\xi)$

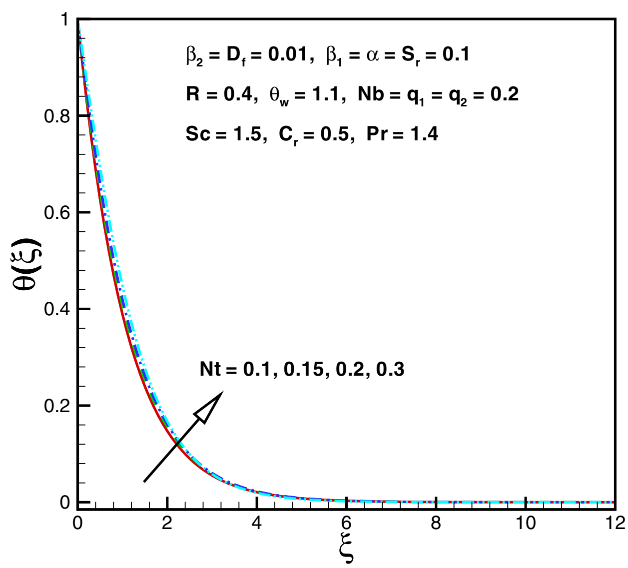

Fig. 7 Impact of Nt on $\theta(\xi)$

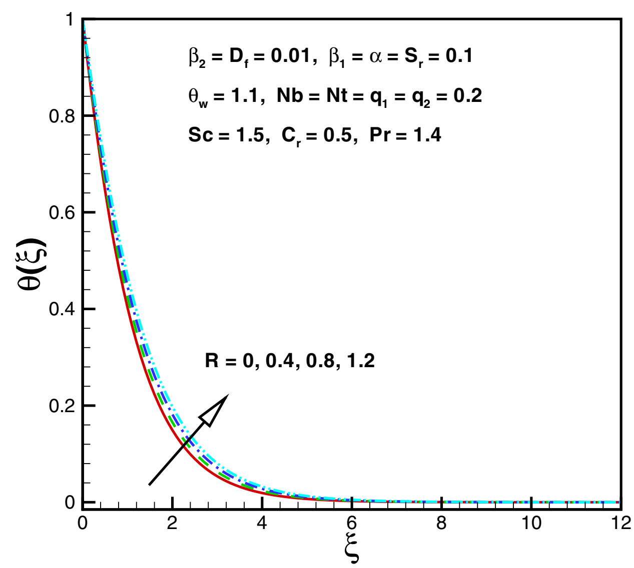

Fig. 9 Impact of R on $\theta(\xi)$

values of (β_1), stress relaxation is less in comparison to the characteristic timescale. Hence, the fluid behavior is closely similar to that of especially solid material. The role of retardation time parameter $(\beta_2 = 1.5,\ 1.6,\ 1.7,\ 1.8)$ on fluid velocity is plotted in Fig. 4. As expected, that motion of fluid increases for larger (β_2). Basically, retardation time refers to time required for the buildup of shear stress in a fluid. Thus, it can show the timescale observation that is not explained by relaxation time. It is clear that flow parallel to the sheet accelerates with an enhancement in fluid retardation time.

Figure 5 highlights the behavior of the curvature parameter $(\alpha = 0,\ 1,\ 2,\ 3)$ for velocity. $f'(\eta)$ is directly proportional to (α), due to the fact that the radius of the cylinder decreases when (α) amplifies. Therefore, fluid motion get experiences with minimum resistance and thus the velocity increases.

Temperature

Figure 6 shows the behavior of Brownian motion parameter $(Nb = 0.1,\ 0.4,\ 0.7,\ 1.1)$ on temperature $\theta(\xi)$. It is observed that the temperature is a decreasing function

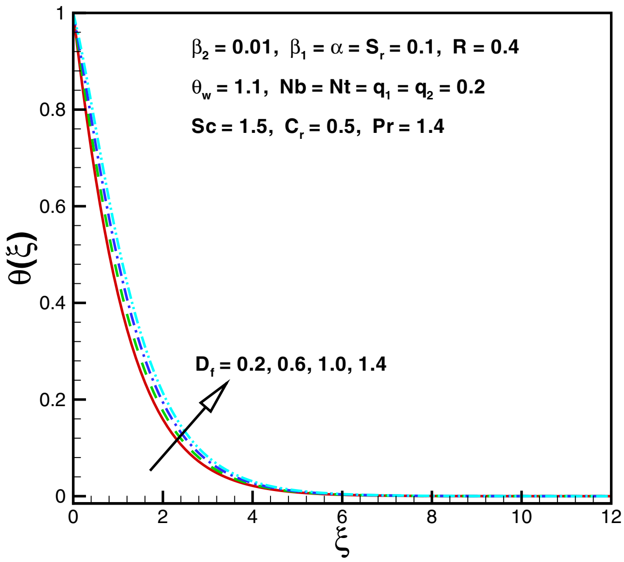

Fig. 10 Impact of D_f on $\theta(\xi)$

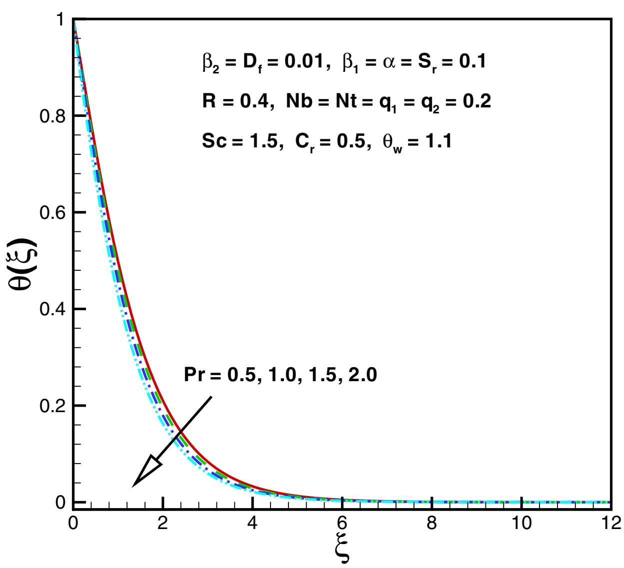

Fig. 11 Impact of Pr on $\theta(\xi)$

of (Nb). For multiple values of ($Nt = 0.1, 0.15, 0.2, 0.3$), the temperature field is depicted in Fig. 7 Physically for higher values of (Nt), an enhancement in thermophoresis force develops which tends to move the nanoparticles from the hot to cold regions. Hence, the temperature rises. Figure 8 shows the influence of temperature ratio parameter $\left(\theta_w = 1.1, 1.3, 1.5, 1.7\right)$ on temperature. It is obvious that an increase in $\left(\theta_w\right)$ enhances the temperature. Higher wall temperature in comparison with the ambient temperature of the fluid is observed due to larger $\left(\theta_w\right)$. Due to this, the temperature of the fluid increases gradually.

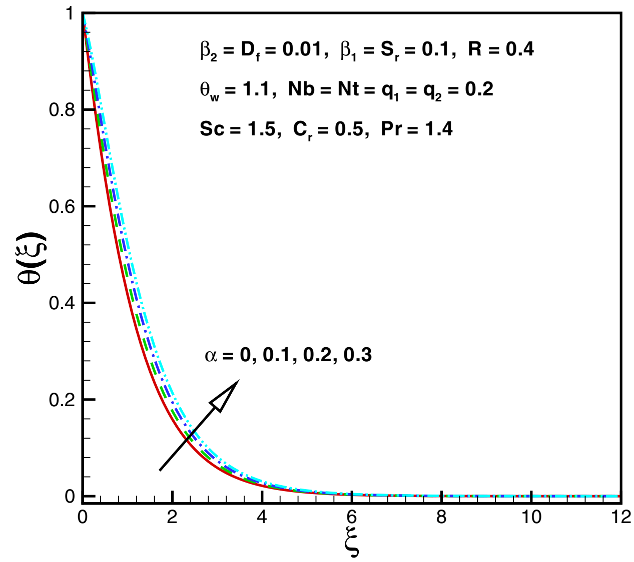

Fig. 12 Impact of α on $\theta(\xi)$

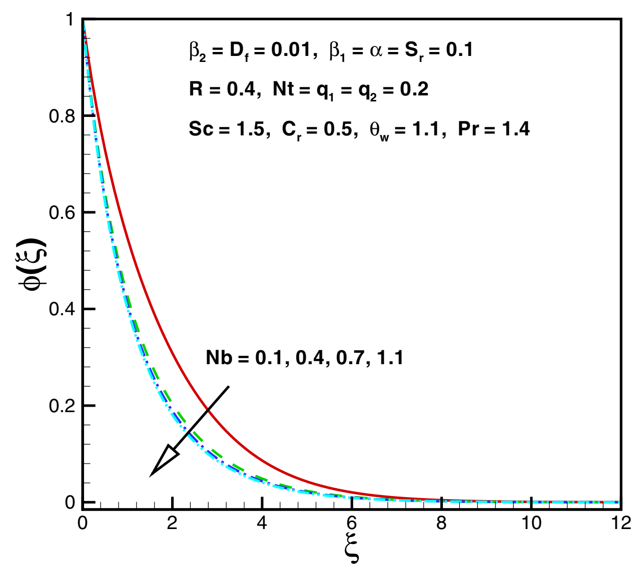

Fig. 13 Impact of Nb on $\phi(\xi)$

Figure 9 provides the analysis for variation of the radiation parameter ($R = 0.0, 0.4, 0.8, 1.2$) on temperature. A rise in temperature curves is observed when (R) is increased. Physically for higher values of (R), the mean absorption coefficient decreases. The existence of a temperature difference is due to diffusion flux. This is a cause of temperature $\theta(\xi)$ enhancement. The temperature profile for different values of Dufour number $\left(D_f = 0.2, 0.6, 1.0, 1.4\right)$ is analyzed in Fig. 10. It depicts that larger values of $\left(D_f\right)$ enhance the temperature field. Figure 11 shows the influence of Prandtl number ($Pr = 0.5, 1.0, 1.5, 2.0$) on

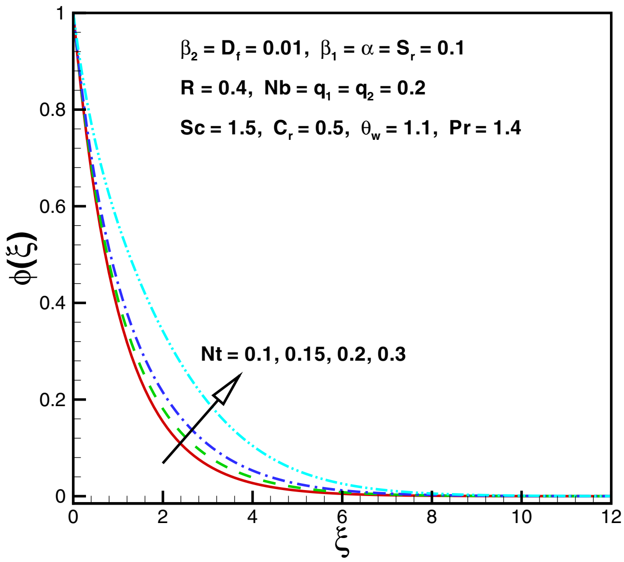

Fig. 14 Impact of Nt on $\phi(\xi)$

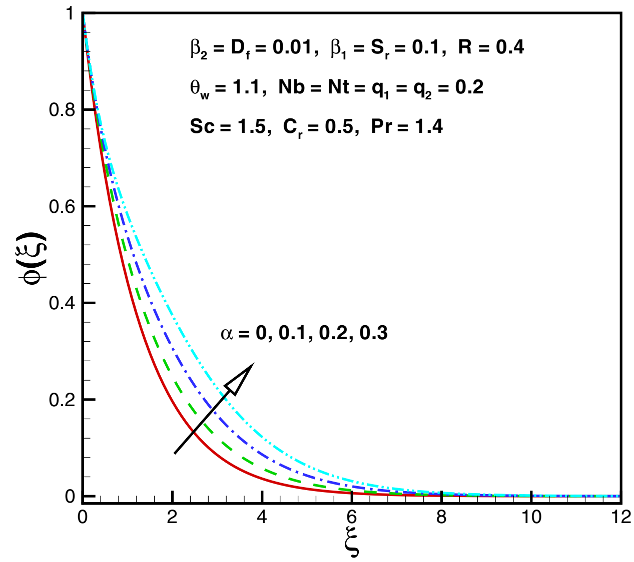

Fig. 16 Impact of α on $\phi(\xi)$

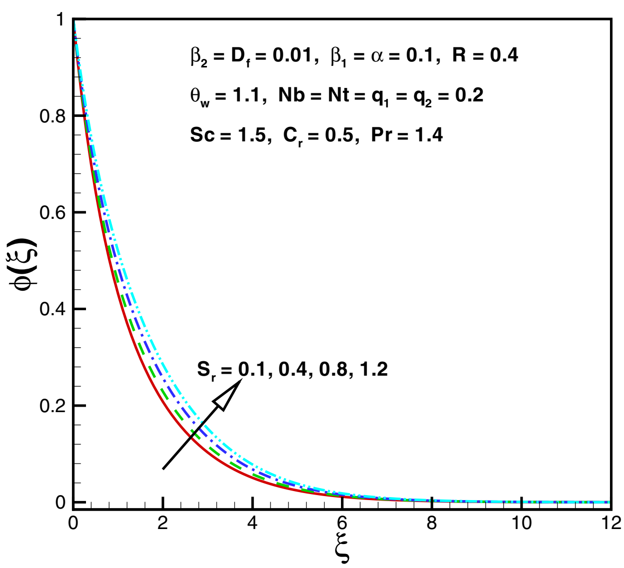

Fig. 15 Impact of S_{r} on $\phi(\xi)$

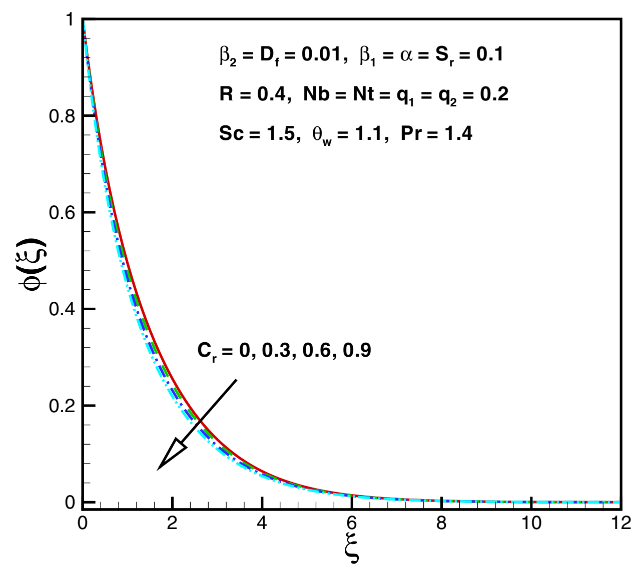

Fig. 17 Impact of C_{r} on $\phi(\xi)$

temperature. For larger values of (Pr), the temperature of the fluid decays. Prandtl number has an inverse relation to thermal diffusivity. Higher Pr creates a weaker thermal diffusivity which causes of reduction of temperature field. Figure 12 shows the influence of curvature parameter $(\alpha = 0,\ 1,\ 2,\ 3)$ on temperature $\theta(\xi)$. It is noted that when (α) increases, the temperature field is enhanced. Physically, the radius of curvature decreases, which reduces the interaction region of the cylinder with the liquid. Hence, the temperature profile increases.

Concentration

The physical aspects for increasing values of Brownian motion $(Nb = 0.1,\ 0.4,\ 0.7,\ 1.1)$ and thermophoresis $(Nt = 0.1,\ 0.15,\ 0.2,\ 0.3)$ are displayed in Figs. 13 and 14. We noted that Nb and Nt have conflicting impact on concentration $\phi(\xi)$. To examine the aspect of Soret number $\left(S_{\mathrm{r}} = 0.1,\ 0.4,\ 0.8,\ 1.2\right)$ on concentration $\phi(\xi)$, Fig. 15 has been prepared. There is an enhancement in the concentration profile for larger values of Sr. Figure 16 shows the impact of the curvature parameter $(\alpha = 0,\ 0.1,\ 0.2,\ 0.3)$ on

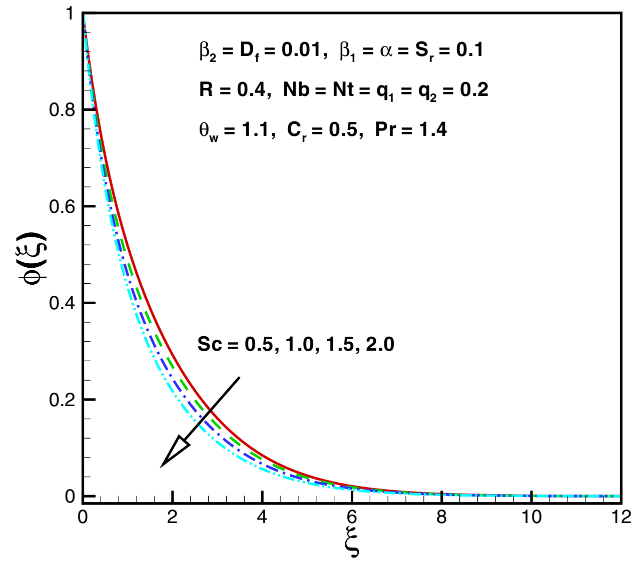

Fig. 18 Impact of Sc on $\phi(\xi)$

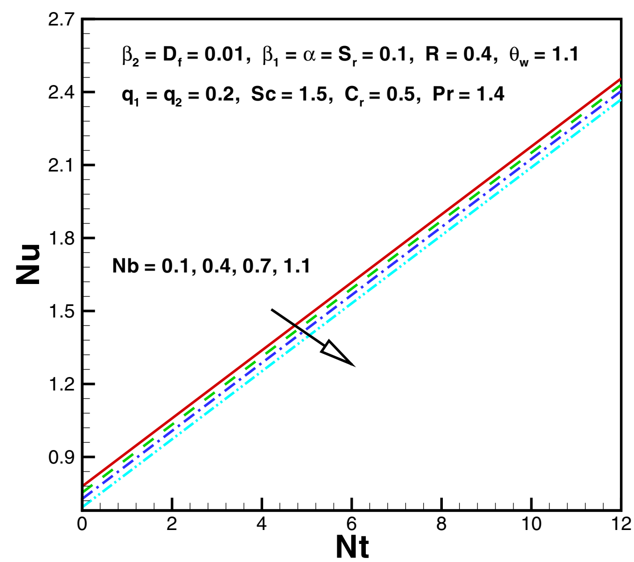

Fig. 19 Impact of Nb on Nu

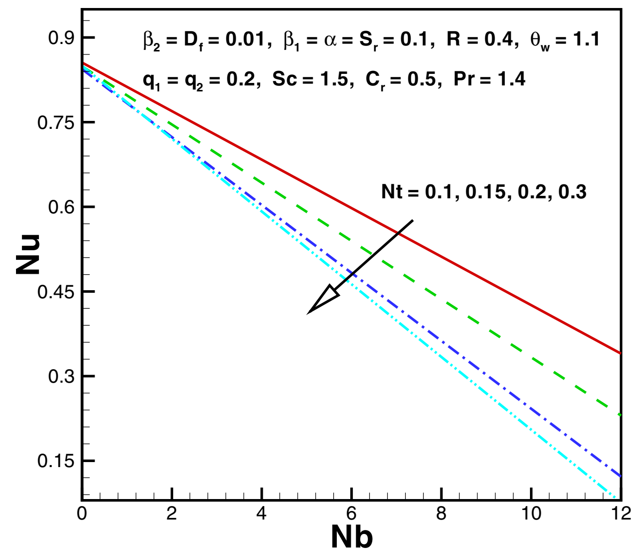

Fig. 20 Impact of Nt on Nu

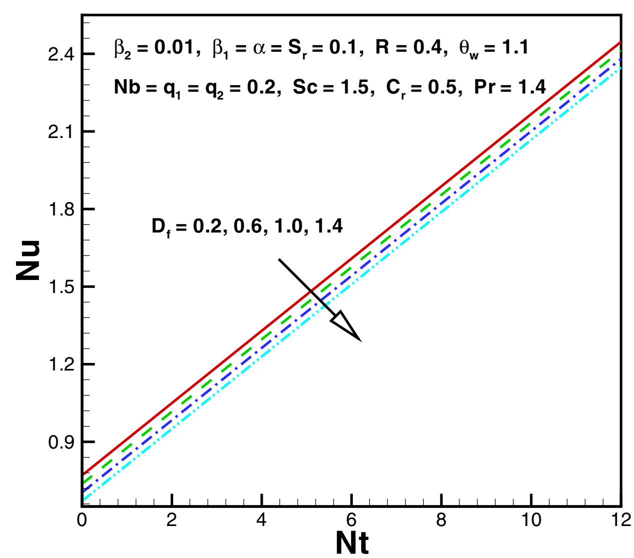

Fig. 21 Impact of D_f on Nu

concentration $\phi(\xi)$. It was reported that the concentration $\phi(\xi)$ increased with higher α. Furthermore, in the case of a flat surface, the concentration boundary layer is dominant when associated with a stretching cylinder. The behavior of the chemical reaction parameter ($C_r = 0, 0.3, 0.6, 0.9$) on concentration $\phi(\xi)$ is plotted in Fig. 17. The concentration $\phi(\xi)$ declines for growing values of C_r. This happens because the species rate decays when C_r intensifies. Hence, the concentration field $\phi(\xi)$ declines. Figure 18 illustrates that the concentration $\phi(\xi)$ declines for higher Schmidt number ($Sc = 0.5, 1.0, 1.5, 2.0$). Physically, smaller mass diffusivity causes a reduction in $\phi(\xi)$ when Sc increases.

Heat transfer rate

The influences of Brownian motion (Nb), thermophoresis parameter (Nt), Dufour number (D_f) and radiation parameter (R) on Nusselt number (Nu) are depicted in Figs. (19, 20, 21 and 22). The heat transfer quantity for higher values of Nb, Nt, D_f and R declines as shown in these plots.

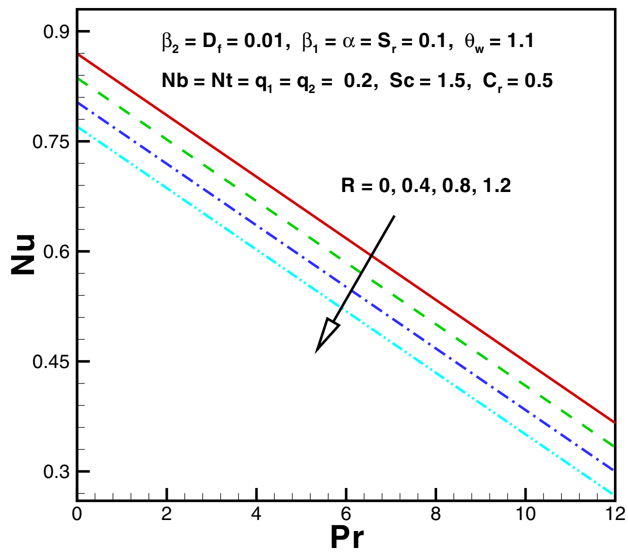

Fig. 22 Impact of R on Nu

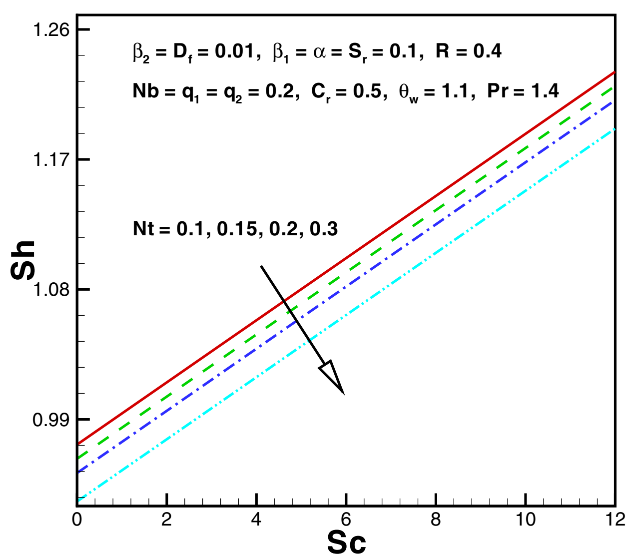

Fig. 23 Impact of Nt on Sh

Mass transfer rate

The behavior of Sherwood number (Sh) for higher values of thermophoresis parameter (Nt) and Soret number $\left(S_r\right)$ indicates a decline in the mass transfer quantity as shown in Figs. (23 and 24).

Major findings

Here, the impact of Soret and Dufour and nonlinear thermal radiation in Oldroyd-B nanofluid is reported by utilizing the optimal homotopic approach. The aspects of

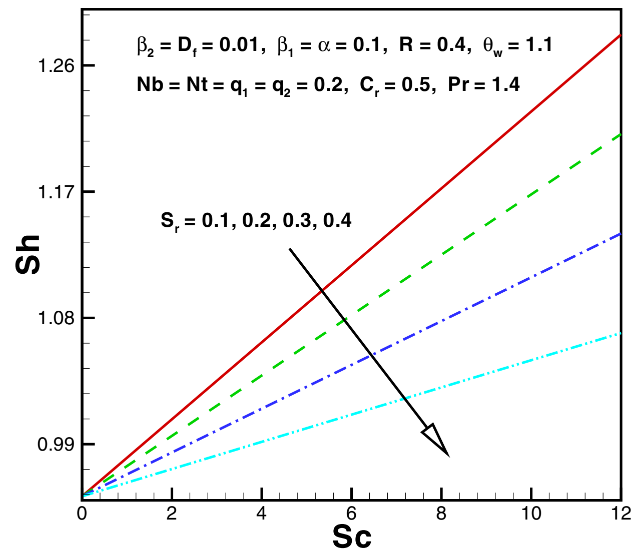

Fig. 24 Impact of S_r on Sh

non-uniform heat sink/source and chemical reaction have been considered. This study indicated that the Deborah numbers (β_1 and β_2) display opposite behavior for the velocity field. The temperature field increased Brownian motion (Nb), thermophoresis (Nt) and curvature (α) parameters. The impacts of Soret number $\left(S_r\right)$ and chemical reaction parameter $\left(C_r\right)$ are totally opposite on the concentration profile. For higher values of Schmidt number, the concentration of the nanofluid decreases. The local Nusselt number decreased for higher radiation parameter (R) and Dufour number $\left(D_f\right)$. An enhancement in thermophoresis (Nt) and Soret number $\left(S_r\right)$ caused the reduction of Sherwood number.

References

Abel MS, Tawade JV, Nandeppanavar MM (2012) MHD flow and heat transfer for the upper-convected Maxwell fluid over a stretching sheet. Meccanica 47:385–393

Alshomrani AS, Irfan M, Saleem A, Khan M (2018) Chemically reactive flow and heat transfer of magnetite Oldroyd-B nanofluid subject to stratifications. Appl Nanosci 8:1743–1754

Anwar MS, Rasheed A (2017) Heat transfer at microscopic level in a MHD fractional inertial flow confined between non-isothermal boundaries. Eur Phys J Plus 132:305

Anwar MS, Rasheed A (2018) Joule heating in magnetic resistive flow with fractional Cattaneo-Maxwell model. J Brazilian Soc Mech Sci Eng 40:501. https://doi.org/10.1007/s40430-018-1426-8

Awais M, Saleem S, Hayat T, Irum S (2016) Hydromagnetic couple-stress nanofluid flow over a moving convective wall: OHAM analysis. Acta Astro 129:271–276

Awais M, Ehsan S, Khalid A, Zuhaib I, Khan A, Raja MAZ (2018) Hydromagnetic mixed convective flow over a wall with variable thickness and Cattaneo-Christov heat flux model: OHAM analysis. Results Phy 8:621–627

Babu MJ, Sandeep N (2016) Three-dimensional MHD slip flow of nanofluids over a slendering stretching sheet with thermophoresis and Brownian motion effects. Adv Powder Tech 27:2039–2050

Bhatnagar RK, Gupta G, Rajagopal KR (1995) Flow of an Oldroyd-B fluid due to a stretching sheet in the presence of a free stream velocity. Int J Non-Linear Mech 30:391–405

Buongiorno J (2006) Convective transport in nnaofluids. ASME J Heat Transf 128:240–250

Choi SUS (1995) Enhancing thermal conductivity of fluids with nanoparticles, ASME, FEC 231/MD, USA, pp 99–105

Farooq A, Ali R, Benimcd AC (2018) Soret and Dufour effects on three dimensional Oldroyd-B fluid. Phys A Stat Mech Appl 503:345–354

Gupta S, Kumar D, Singh J (2018) MHD mixed convective stagnation point flow and heat transfer of an incompressible nanofluid over an inclined stretching sheet with chemical reaction and radiation. Int J Heat Mass Transf 118:378–387

Hayat T, Khan MWA, Alsaedi A, Ayub M, Khan MI (2017) Stretched flow of Oldroyd-B fluid with Cattaneo-Christov heat flux. Results Phys 7:2470–2476

Hayat T, Shah F, Khan MI, Alsaedi A (2018a) Numerical simulation for aspects of homogeneous and heterogeneous reactions in forced convection flow of nanofluid. Results Phys 8:206–212

Hayat T, Aziz A, Muhammad T, Alsaedi A (2018b) An optimal analysis for Darcy–Forchheimer 3D flow of nanofluid with convective condition and homogeneous–heterogeneous reactions. Phys Lett A 382:2846–2855

Hayat T, Rashid M, Alsaedi A (2018c) Three dimensional radiative flow of magnetite-nanofluid with homogeneous-heterogeneous reactions. Results Phys 8:268–275

Irfan M, Khan M (2019) Simultaneous impact of nonlinear radiative heat flux and Arrhenius activation energy in flow of chemically reacting Carreau nanofluid. Appl Nanosci

Irfan M, Khan M, Khan WA, Sajid M (2018) Thermal and solutal stratifications in flow of Oldroyd-B nanofluid with variable conductivity. Appl Phys A 124:674. https://doi.org/10.1007/s00339-018-2086-3

Khan M, Irfan M, Khan WA (2017) Impact of nonlinear thermal radiation and gyrotactic microorganisms on the Magneto-Burgers nanofluid. Int J Mech Sci 130:375–382

Khan MI, Hayat T, Khan MI, Alsaedi A (2018) Activation energy impact in nonlinear radiative stagnation point flow of cross nanofluid. Int Comm Heat Mass Transf 91:216–224

Khan M, Irfan M, Khan WA, Sajid M (2019) Consequence of convective conditions for flow of Oldroyd-B nanofluid by a stretching cylinder. J Brazilian Soc Mech Sci Eng. https://doi.org/10.1007/s40430-019-1604-3

Madavan R, Kumar SS, Iruthyarajan MW (2018) A comparative investigation on effects of nanoparticles on characteristics of natural esters-based nanofluids. Colloids Surf A Physicochem Eng 556:30–36

Megahed AM (2013) Variable fluid properties and variable heat flux effects on the flow and heat transfer in a non-Newtonian Maxwell fluid over an unsteady stretching sheet with slip velocity. Chin Phys B 22:094701

Minakov AV, Rudyak VY, Pryazhnikov MI (2018) Rheological behavior of water and ethylene glycol based nanofluids containing oxide nanoparticles. Colloids Surf A Physicochem Eng 554:279–285

Mudhaf AF, Rashad AM, Ahmed SE, Chamkha AJ, Kabeir SMME (2018) Soret and Dufour effects on unsteady double diffusive natural convection in porous trapezoidal enclosures. Int J Mech Sci 140:172–178

Munyalo JM, Zhang X (2018) Particle size effect on thermophysical properties of nanofluid and nanofluid based phase change materials: a review. J Mol Liq 265:77–87

Muthtamilselvan M, Periyadurai K, Doh DH (2018) Impact of nonuniform heated plate on double-diffusive natural convection of micropolar fluid in a square cavity with Soret and Dufour effects. Adv Powder Tech 29:66–77

Nishimura T, Wakamatsu M, Morega AM (1998) Oscillatory double-diffusive convection in a rectangular enclosure with combined horizontal temperature and concentration gradients. Int J Heat Mass Transf 41:1601–1611

Rasheed A, Anwar MS (2018) Simulations of variable concentration aspects in a fractional nonlinear viscoelastic fluid flow. Commun Nonlinear Sci Numer Simul 65:216–230

Rasheed A, Anwar MS (2019) Interplay of chemical reacting species in a fractional viscoelastic fluid flow. J Mol Liq 273:576–588

Reddy S, Naikoti K, Rashidi MM (2017) MHD flow and heat transfer characteristics of Williamson nanofluid over a stretching sheet with variable thickness and variable thermal conductivity. Trans A Razmadze Math Inst 171:195–211

Zhang Y, Yuan B, Bai Y, Cao Y, Shen Y (2018) Unsteady Cattaneo-Christov double diffusion of Oldroyd-B fluid thin film with relaxation-retardation viscous dissipation and relaxation chemical reaction. Powder Tech 338:975–998

Publisher's Note Springer Nature remains neutral with regard to jurisdictional claims in published maps and institutional affiliations.